



1 Development of high-resolution Thermosphere-Ionosphere 2 Electrodynamics General Circulation Model (TIE-GCM) using Ring 3 Average technique

4 **Tong Dang**^{1,2,3,5}, **Binzheng Zhang**^{4,5}, **Jiuhou Lei**^{1,2,3,*}, **Wenbin Wang**⁵, **Alan Burns**⁵, **Han-li Liu**⁵,
5 **Kevin Pham**⁵, **Kareem A. Sorathia**⁶

6 ¹CAS Key Laboratory of Geospace Environment, School of Earth and Space Sciences, University of Science and Technology of
7 China, Hefei, China

8 ²Mengcheng National Geophysical Observatory, University of Science and Technology of China, Hefei, China

9 ³CAS Center for Excellence in Comparative Planetology, Hefei, China

10 ⁴Department of Earth Sciences, the University of Hong Kong, Pokfulam, Hong Kong SAR, China

11 ⁵High Altitude Observatory, National Center for Atmospheric Research, Boulder, CO, USA

12 ⁶Applied Physics Laboratory, Johns Hopkins University, Laurel, MD, USA

13 *Corresponding author: Jiuhou Lei, leijh@ustc.edu.cn

14 **Abstract.** When solving hydrodynamic equations in spherical/cylindrical geometry using explicit finite difference schemes, a
15 major difficulty is that the time step is greatly restricted by the clustering of azimuthal cells near the pole due to the Courant-
16 Friedrichs-Lewy condition. This paper adapts the azimuthal averaging-reconstruction (Ring Average) technique to finite differ-
17 ence schemes in order to mitigate the time step constraint in spherical/cylindrical coordinates. The finite-difference Ring Average
18 technique averages physical quantities based on an effective grid and then reconstructs the solution back to the original grid in a
19 piece-wise, monotonic way. The algorithm is implemented in a community upper atmospheric model Thermosphere-Ionosphere
20 Electrodynamics General Circulation Model (TIE-GCM), with horizontal resolution up to $0.625^\circ \times 0.625^\circ$ in the geographic
21 longitude-latitude coordinates, which enables the capability of resolving critical mesoscale structures within the TIE-GCM. Nu-
22 merical experiments have shown that the Ring Average technique introduces minimal artifacts in the polar region of the GCM
23 solutions, which is a significant improvement compared to the commonly used low-pass filtering techniques such as the fast
24 Fourier transform method. Since the finite-difference adaptation of the Ring Average technique is a post-solver type algorithm,
25 which requires no changes to the original computational grid and numerical algorithms, it has also been implemented in much
26 more complicated models with extended physical/chemical modules such as the coupled Magnetosphere Ionosphere Thermo-
27 sphere (CMIT) model and the Whole Atmosphere Community Climate Model with thermosphere and ionosphere extension
28 (WACCM-X). The implementation of the Ring Average techniques in both models enables CMIT and WACCM-X to perform
29 global simulations with a much higher resolution than that used in the community versions. The new technique is not only a
30 significant improvement in space weather modeling capability, but can also be adapted to more general finite difference solvers
31 for hyperbolic equations in spherical/polar geometries.

32 **Key Points:**

- 33 • Ring Average technique is adapted to solve the issue of clustered grid cells in polar/spherical coordinate with finite
34 difference method.
- 35 • The Ring Average technique is applied to develop a $0.625^\circ \times 0.625^\circ$ high-resolution TIE-GCM and more complicated
36 geoscientific models.
- 37 • The high-resolution TIE-GCM shows good capability in resolving mesoscale structures in the I-T system.

38 **Keywords:** Finite difference method, Spherical geometry, Ionosphere-thermosphere system, General circulation model, CFL
39 condition.



40 1 Introduction

41 Mesoscale structures with typical horizontal size of 100~500 km, have gained more and more attention
42 in the research of the dynamics of the upper atmospheric system. A number of studies have been carried
43 out to investigate these structures, including the formation and evolution of polar cap patches and tongues
44 of ionization [Basu et al., 1995; Foster et al., 2005; Zhang et al., 2013], dynamics of ionospheric irreg-
45 ularities [Makela and Otsuka, 2012; Sun et al., 2015], variations of polar thermospheric density anomaly
46 [Crowley et al., 2010; Lühr et al., 2004], and the space weather effects of mesoscale electric field vari-
47 ability [Codrescu et al., 1995; Matsuo and Richmond, 2008; Zhu et al., 2018; Lotko and Zhang, 2018].
48 These dynamic mesoscale structures have shown critical importance in both understanding the physics of
49 the solar-terrestrial system and space weather predictions, which challenges the resolution and accuracy of
50 numerical models of the upper atmospheric system in resolving these important mesoscale signatures.

51 Spherical or cylindrical coordinates are commonly used in solving geophysical problems, including
52 the modeling of the upper atmospheric systems. As a workhorse for space weather research, a number
53 of global circulation models (GCMs) for the coupled ionosphere-thermosphere (I-T) system have been
54 developed based on spherical coordinates using finite difference schemes [e.g., Richmond et al., 1992;
55 Fuller-Rowell et al., 1996; Ridley et al., 2006; Ren et al., 2009]. However, restricted by the longitudinal
56 grid resolution, current horizontal resolutions used in I-T GCMs are still insufficient for fully resolving
57 mesoscale atmospheric structures, which are either marginal or sub-grid. The latest released version of the
58 community code, Thermosphere Ionosphere Electrodynamic General Circulation Model (TIE-GCM), has a
59 longitude-latitude resolution of $2.5^\circ \times 2.5^\circ$; the Coupled Thermosphere/Ionosphere Plasmasphere (CTIP)
60 Model has a latitude resolution of 2° and a longitude resolution of 18° ; the most recent version of the Global
61 Ionosphere Thermosphere Model (GITM) has a flexible grid with latitudinal resolution up to 0.3125° but the
62 typical longitudinal resolution remains 2.5° due to severe time step restrictions for global-scale calculations.

63 The major difficulty in increasing longitudinal resolution in spherical geometry based GCMs is that the
64 explicit time stepping is constrained by the clustering azimuthal cells near the pole due to the Courant-
65 Friedrichs–Lewy (CFL) condition [Courant et al., 1928]. A number of attempts have been proposed to
66 address this coordinate singularity issue ([e.g., Purser, 1988; Bouaoudia and Marcus, 1991; Williamson
67 et al., 1992; Takacs, 1999; Fukagata and Kasagi, 2002; Prusa, 2018]). To use a time step that is larger than
68 the global minimum requirement from the CFL conditions, one common method used in a spherical GCM
69 is to employ a low-pass Fourier filter at polar latitudes, which removes non-physical, high-frequency zonal



70 waves generated due to numerical instability caused by the local violation of the CFL conditions [e.g., Ska-
71 marock et al., 2008]. Although the Fourier filter can maintain the computational stability and permit a much
72 larger temporal step, the applicability of the Fast Fourier Transform (FFT) filter method is problem depen-
73 dent, which also bring barriers in moving models forward to finer spatial resolutions. Moreover, the linear
74 filtering of zonal components generated through a non-physical time step may decrease the accuracy of the
75 model calculations near the polar region, which affects physical conservations of e.g. mass, momentum and
76 energy that are essential for long-term behavior of the GCM [Williamson and Browning, 1973].

77 Recently, Zhang et al. [2019] developed a new technique named the “Ring Average” method for hy-
78 perbolic equations to mitigate the CFL restrictions in spherical polar geometry, on the basis of the method
79 originally proposed in the Lyon-Fedder-Mobarry (LFM) MHD simulations [Lyon et al., 2004]. The method
80 is a “post-solver” type algorithm applied after solving all the physical quantities in the original spherical
81 polar coordinates, thus no modification to either the numerical solver or the computational grid is required
82 when applying the Ring Average. Test simulation results have shown the effectiveness of the Ring Average
83 algorithm in increasing the time step by a factor of 100 while maintaining the fidelity of the solutions. The
84 original Ring Average technique was developed for solving hyperbolic equations in spherical/polar geom-
85 etry based on finite volume schemes, which redistributes the solution azimuthally through a conservative
86 averaging-reconstruction algorithm. The finite-volume version of the Ring Average technique not only re-
87 leases the time step constraint in spherical geometry, but also keeps the conservative nature of finite-volume
88 schemes to machine precision. In this paper, we adapt the Ring Average technique to finite difference
89 schemes for solving hyperbolic equations. Defined on an effective reduced polar grid, the finite-difference
90 adaption of the Ring Average technique also conducts a “post-solver” step of averaging-reconstruction in
91 each azimuthal ring to maintain the numerical stability and relax the severe computational time step con-
92 straint. To demonstrate the effectiveness of the finite-difference version of the Ring Average technique,
93 we use solutions from both linear advection equations and the TIE-GCM as test beds. The Ring Average
94 algorithm enables the use of high-resolution TIE-GCM such as $0.625^\circ \times 0.625^\circ$ in longitude and latitude
95 with reasonable time steps and minimal numerical artifacts. Further applications of the technique on cou-
96 pled Magnetosphere Ionosphere Thermosphere (CMIT) and Whole Atmosphere Community Climate Model
97 with thermosphere and ionosphere extension (WACCM-X) are also addressed.

98 This paper is organized as follows: In Section 2, we describe the details of the model and the Ring
99 Average technique to solve the clustering of polar grid cells problem. A hydrodynamic convection experi-



100 ment with the Ring Average technique has also been conducted to test the capability of the method. Section
101 3 shows the preliminary results of the high-resolution TIE-GCM with the Ring Average technique imple-
102 mented as well as the further applications of the technique. The findings of this work are summarized in
103 Section 4.

104 **2 Methodology**

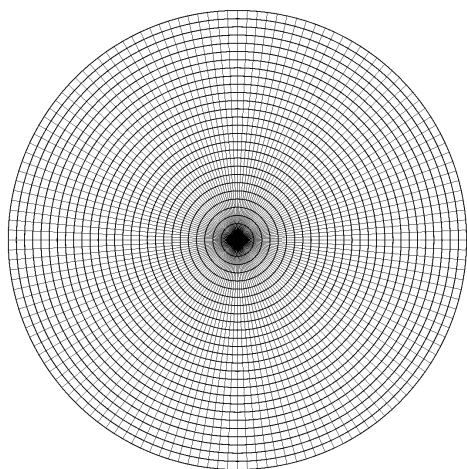
105 *2.1 Ring Average in the Finite-Difference Form*

106 An example of the standard polar grids with a horizontal resolution of $2.5^\circ \times 2.5^\circ$ (longitude \times latitude)
107 in the TIE-GCM is shown in Figure 1. It is evident that in Figure 1a, the azimuthal (longitudinal) com-
108 putational nodes in the standard polar grid are significantly clustered near the pole even with 144 cells in
109 the azimuthal direction, resulting in very “thin” cells with small azimuthal extensions which restricts the
110 explicit time step for the advection equations. This azimuthal clustering becomes even worse when grid
111 resolution increases, namely the time step drops to 1/4 while the grid resolution doubles, corresponding
112 to at least 32 times increases in computational resource, which becomes expensive especially for global
113 simulations with high spatial resolutions in order to resolve mesoscale structures.

114 The finite difference adaption of the Ring Average algorithm is based on a similar averaging-reconstruction
115 process over a pre-defined, “effective” azimuthal grid as used in the finite-volume version of the algorithm.
116 Figure 1b shows an example of “effective” polar grid for applying the finite-difference Ring Average tech-
117 nique. In the polar grid shown in Figure 1b, since the reconstructed solution is monotonic within each
118 effective computational cell, a much larger time step is allowed compared to the original grid shown in
119 Figure 1a. As shown in Figure 1b, the effective longitudinal grid resolutions have been reduced and are
120 less clustered towards the pole. For the most inside (highest latitude) grids, the 144 azimuthal cells (Figure
121 1a) have been grouped to 9 effective cells (chunks), with 16 original cells in each chunk. Moving away
122 from the pole, more chunks are employed. As an example, the numbers of chunks from inside to outside
123 shown in Figure 1b in the effective grid are 9, 9, 18, 18, 36, 36, 72, 72, 72, and 72, respectively, allowing
124 a relative smooth transition in the size of the cells going radially outward. Note that the choice of the num-
125 ber of chunks in each ring is non-unique. Numerical tests with the Finite-Volume solvers have shown that
126 the computational solution, under both smooth and discontinuous flow conditions, is insensitive to small
127 changes in the chunk configuration [Zhang et al., 2019].



(a) Original Polar Grid



(b) Effective Grid

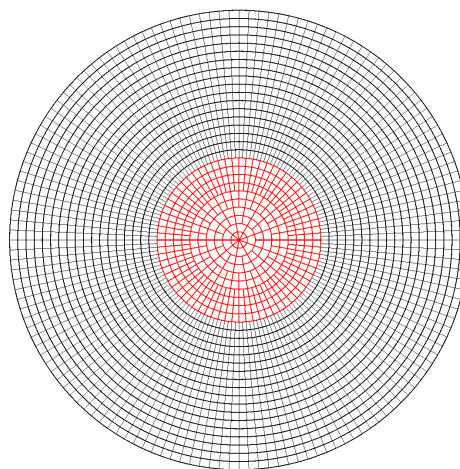


Fig 1 The (a) original and (b) effective $2.5^\circ \times 2.5^\circ$ TIE-GCM polar longitude-latitude grid.

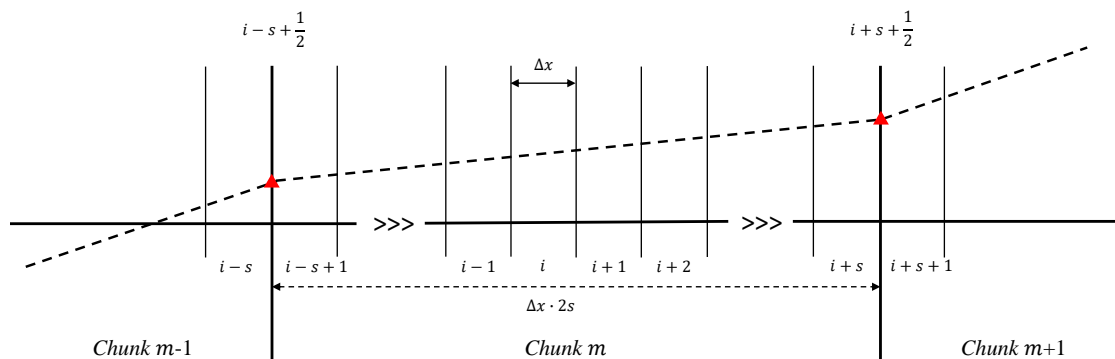


Fig 2 Schematic of grid cells within effective chunks

128 We use the following example of solving the linear advection equation to illustrate the averaging-
 129 reconstruction process within each chunk. Consider the following linear advection equation of an incom-
 130 pressible fluid in the azimuthal direction as an example:

131
$$\frac{\partial \rho}{\partial t} + v \frac{\partial \rho}{\partial x} = 0, \quad (1)$$



132 where v is the advection velocity, ρ is the density profile, and x is the azimuthal dimension ($x \in [0, 2\pi)$)
 133 along one ring. Assuming the x direction is uniformly discretized into N_{total} computational cells with
 134 $\Delta x = \frac{2\pi}{N_{total}}$, a central difference Euler form of Equation (1) for density ρ in cell k between time n and $n + 1$
 135 is written as

$$136 \quad \frac{1}{\Delta t} (\rho_k^{n+1} - \rho_k^n) = -\frac{v}{2\Delta x} (\rho_{k+1}^n - \rho_{k-1}^n), \quad (2)$$

137 where k denotes the index of an individual “thin” cell in the original azimuthal grid. Δt is the time step
 138 regulated by the CFL condition. Without ring average type of treatment, the time step Δt is restricted
 139 by the fact that “thin” azimuthal cells cluster near the pole. The ring average technique takes the average
 140 solution within a chunk m that contains $2s$ cells in the original grid as shown in Figure 2. Summing over
 141 the finite-difference form of Equation (1) within chunk m gives:

$$142 \quad \sum_{k=i-s+1}^{i+s} \frac{1}{\Delta t} (\rho_k^{n+1} - \rho_k^n) = -\frac{v}{2\Delta x} \sum_{k=i-s+1}^{i+s} (\rho_{k+1}^n - \rho_{k-1}^n). \quad (3)$$

143 Then summing over the k indices within chunk m , Equation (3) becomes:

$$144 \quad \frac{1}{\Delta t} \left(\sum_{k=i-s+1}^{i+s} \rho_k^{n+1} - \sum_{k=i-s+1}^{i+s} \rho_k^n \right) = -\frac{v}{2\Delta x} \sum_{k=i-s+1}^{i+s} [(\rho_{k+1}^n - \rho_k^n) + (\rho_k^n - \rho_{k-1}^n)] \quad (4)$$

$$145 \quad = -\frac{v}{2\Delta x} [(\rho_{i+s+1}^n - \rho_{i-s+1}^n) + (\rho_{i+s}^n - \rho_{i-s}^n)] \quad (5)$$

$$146 \quad = -\frac{v}{\Delta x} \left(\frac{\rho_{i+s+1}^n + \rho_{i+s}^n}{2} - \frac{\rho_{i-s+1}^n + \rho_{i-s}^n}{2} \right) \quad (6)$$

$$147 \quad = -\frac{v}{\Delta x} \left(\rho_{i+s+\frac{1}{2}}^n - \rho_{i-s+\frac{1}{2}}^n \right), \quad (7)$$

148 where $\rho_{i-s+\frac{1}{2}}^n$ and $\rho_{i+s+\frac{1}{2}}^n$ are the left- and right-values on the boundary of chunk m , as indicated by the red
 149 triangles in Figure 2. The LHS of Equation (7) is basically the time rate of the change in terms of the chunk
 150 density ϱ_m :

$$151 \quad \frac{1}{\Delta t} (\varrho_m^{n+1} - \varrho_m^n), \quad (8)$$

152 where $\varrho_m^{n+1} = \sum_{k=i-s+1}^{i+s} \rho_k^{n+1}$ and $\varrho_m^n = \sum_{k=i-s+1}^{i+s} \rho_k^n$. If assuming smoothness of the solution which
 153 applies to typical upper atmospheric flow conditions, and using a piece-wise linear reconstruction for the



154 two interface values at time level n :

155
$$\rho_{i+s+\frac{1}{2}}^n = \frac{\varrho_{m+1} + \varrho_m}{2} \quad (9)$$

156
$$\rho_{i-s+\frac{1}{2}}^n = \frac{\varrho_m + \varrho_{m-1}}{2}, \quad (10)$$

157 the RHS of Equation (7) is in the form of a central difference approximation of the spatial derivative $\frac{\partial \varrho}{\partial x}$ in
158 chunk m :

159
$$-\frac{v}{\Delta x} \frac{\varrho_{m+1}^n - \varrho_{m-1}^n}{2}. \quad (11)$$

160 Equating Equation (8) and Equation (11) and considering the fact that the ΔX in computing the chunk
161 derivative is actually $2s\Delta x$, we obtain:

162
$$\frac{1}{\Delta T} (\varrho_m^{n+1} - \varrho_m^n) = -v \frac{\varrho_{m+1}^n - \varrho_{m-1}^n}{2\Delta X}, \quad (12)$$

163 where $\Delta T = 2s\Delta t$. Equation (12) is in the same numerical differential form of the advection equation in
164 terms of the chunk density ϱ in the effective grid, within the same order of finite difference approximation:

165
$$\frac{\partial \varrho}{\partial t} = -v \frac{\partial \varrho}{\partial x} + \mathcal{O}(\Delta X^2). \quad (13)$$

166 Equation (12) also suggests that in principle the ring average method is capable of using a time step that
167 is approximately $2s$ times larger than the original Δt restricted by the “thin” cells (assuming the CFL
168 condition is dominated by the azimuthal direction in the innermost ring). Note that the above derivation
169 of the finite-difference version of the Ring Average algorithm is independent of the numerical schemes
170 solving the linear advection equation (1). Thus, the Ring Average algorithm requires no modifications to
171 the existing hydrodynamic equations solved by GCMs. On the other hand, since the Ring Average algorithm
172 is applied after all the variables are solved on the original spherical grid, it requires no changes to the existing
173 computational grid.

174 In the reconstruction step, the above algorithm uses the piecewise linear method (PLM) to reconstruct
175 solutions within each chunk for the next time step of the GCM calculations, resulting in a 2^{nd} -order accuracy.
176 To achieve higher accuracy in the reconstruction step, a piecewise parabolic reconstruction method (PPM)
177 [Colella and Woodward, 1984] may be used in the algorithm, which provides a 4^{th} -order accuracy for the



178 reconstruction step. In the following section when applying the Ring Average algorithm in a GCM, we
 179 use both PPM and PLM for different variables. The criteria using PPM or PLM here depends on their
 180 spatial gradient from the fluid calculations. For variables which have relatively greater spatial gradient, we
 181 use PPM method to reach a high accuracy and maintain the stability, otherwise the PLM is used for the
 182 calculations.

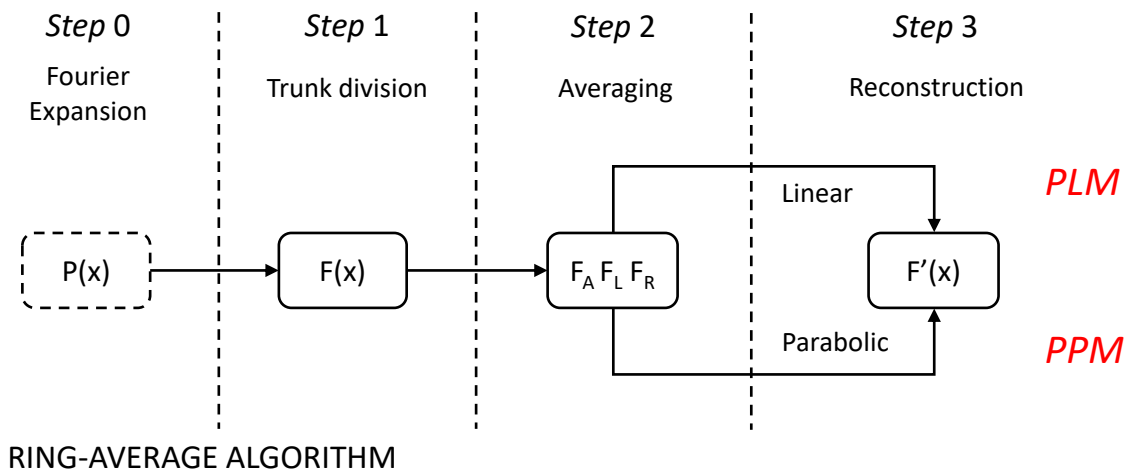


Fig 3 The Ring Average Algorithm with both PLM and PPM methods

183 The algorithm shown in Figure 3 illustrates the steps of applying the Ring Average technique using either
 184 PLM or PPM. The steps consist of chunk division, chunk averaging and reconstruction. The averaging-
 185 reconstruction process (Ring Average) in this study is similar to Zhang et al. [2019], with modifications on
 186 the reconstruction method (PPM or PLM) adapted to finite difference schemes. The detailed procedures of
 187 Ring Average technique in this study are described as follows:

188 *For variables using the PLM reconstruction*

189 *Step 1.* Divide the azimuthal grid cells into chunks and pull data into the chunks.

190 *Step 2.* Calculate the average value F_A , left interface value F_L , and right interface value F_R at chunk
 191 m (m is the index of the chunk number in an azimuthal ring). F_L and F_R are the interface values in each



192 chunk and determined by the following parabola functions:

$$193 \quad F_L = (-F_{m-2} + 7F_{m-1} + 7F_m - F_{m+1})/12 \quad (14)$$

$$194 \quad F_R = (-F_{m-1} + 7F_m + 7F_{m+1} - F_{m+2})/12, \quad (15)$$

195 where F_{m-2} , F_{m-1} , F_m , F_{m+1} , and F_{m+2} are the average values F_A at chunks with index of $m - 2$, $m - 1$,
196 m , $m + 1$, $m + 2$, respectively.

197 *Step 3.* Reconstruct the variables by interpolating the average data linearly in each chunk:

$$198 \quad F_k = \left(1 - \frac{k}{N}\right)F_L + \frac{k}{N}F_R, \quad (16)$$

199 where N is the number of cells within each chunk and k is the local index ranging from 1 to N .

200 *Step 4.* Re-do the above procedures to the next azimuthal ring until ring average is not needed.

201 *For variables using the PPM reconstruction*

202 The procedures in PPM are the same with PLM except for *Step 3*.

203 *Step 3.* Reconstruct the variables parabolically in each chunk using the following function:

$$204 \quad F_k = \frac{A}{3N^2}(3k^2 - 3k + 1) + \frac{B}{2N}(2k - 1) + C, \quad (17)$$

205 where A , B , and C are constants representing the parabolic function which connects F_L and F_R :

$$\begin{aligned} 206 \quad A &= 3(F_L - F_R - 2F_A) \\ B &= 2(3F_A - 2F_L - F_R) \\ C &= F_L. \end{aligned} \quad (18)$$

207 *For vector variables using the PLM reconstruction and Fourier reduction*

208 The “*Step 0*” in Figure 3 corresponds to a Fourier expansion (reduction) step that is required for vector
209 GCM variables in spherical coordinates before applying the Ring Average process. The main purpose of
210 the Fourier reduction step is to maintain the direction of vectors after Ring Average, especially for the
211 neutral meridional and zonal wind across the pole. Thus only the second and higher Fourier components of



212 the data in the azimuthal cell is smoothed using the Ring Average filter, while the zeroth and first Fourier
213 components are kept unchanged. Here are the details of the Fourier expansion process:

214 *Step 0.* Calculate the Fourier components of the azimuthal data:

$$215 \quad P_i = A_0 + A_1 \cos(2\pi i/N_{total}) + B_1 \sin(2\pi i/N_{total}) + F_i, \quad (19)$$

216 where i is the thin cell index along the azimuthal direction ranging from 1 to N_{total} , where N_{total} is the total
217 thin cell number in the azimuthal direction, F_i is the second and higher Fourier components which will be
218 later reconstructed, A_0 , A_1 , B_1 are the zero and first Fourier coefficients:

$$219 \quad \begin{aligned} A_0 &= \frac{1}{L} \sum_{i=1}^{i=L} P_i \\ A_1 &= \frac{1}{L} \sum_{i=1}^{i=L} P_i \cos(2\pi i/L) \\ B_1 &= \frac{2}{L} \sum_{i=1}^{i=L} P_i \sin(2\pi i/L). \end{aligned} \quad (20)$$

220 The higher Fourier components F_i are pulled into chunks for the Ring Average processes.

221 *Step 1-4:* Same with the above PLM methods, except that the reconstructed data F'_i is brought back
222 together with the first two Fourier components after the reconstruction:

$$223 \quad P_i = A_0 + A_1 \cos(2\pi i/L) + B_1 \sin(2\pi i/L) + F'_i. \quad (21)$$

224 2.2 Ring Average for the Advection Equation

225 In this section, in order to illustrate the implementation of the Ring Average algorithm in a finite dif-
226 ference code, we solve the two-dimensional (2D) linear advection equation in the polar geometry as an
227 example. The code used in the 2D linear advection solver is a main subroutine used in the Ring Average
228 module for the GCMs. This two-dimensional advection test in polar geometry is also useful to demonstrate
229 the effectiveness of the finite-difference Ring Average technique in handling a strong, narrow shear flow
230 near the pole. A fourth-order central finite difference scheme is used to solve the following mass continuity



231 equation under the incompressible assumption:

$$232 \quad \frac{\partial \rho}{\partial t} + \mathbf{u} \cdot \nabla \rho = 0, \quad (22)$$

233 where ρ is the density, and \mathbf{u} is the time-stationary flow velocity defined in polar coordinate (r, θ) . The polar
234 geometry of this test is defined with a resolution of 0.625° in both longitude and latitude, with 144 cells in
235 the r -direction uniformly distributed between $(0, 1)$ and 576 cells in the θ -direction uniformly distributed
236 between $(0, 2\pi)$.

237 Figure 4a shows the initial state ($t = 0$) of ρ , ranging linearly along the y direction from a magnitude of
238 2 at the topside to 0.01 at the bottomside:

$$239 \quad \rho = \begin{cases} 2 & y \geq 0.65 \\ (y - 0.65)/(0.65 + 1) * (2 - 0.01) + 2 & y < 0.65. \end{cases} \quad (23)$$

240 The time-independent flow velocity \mathbf{u} is set as a Gaussian-distributed shear flow towards $-y$ and centered
241 at $x = 0.15$ with a peak velocity of -1 and a half width of 0.01 :

$$242 \quad u = -\exp\left[-\frac{(x - 0.15)^2}{0.01}\right]. \quad (24)$$

243 As simulation time evolves, a large density gradient occurs near the pole driven by the time-stationary shear
244 flow, with its pattern following the analytical distribution of the flow velocity \mathbf{u} . Figures 4a-4c show three
245 snapshots of the density in the linear advection experiment at $t = 0$, $t = 0.75$, and $t = 1.5$ using the finite
246 difference version of the Ring Average technique with PPM reconstructions, as described in Section 2.1.
247 For comparisons, Figures 4d-4f show the corresponding snapshots derived from another simulation using an
248 FFT filter, and Figures 4g-4i show the results at the same simulation time calculated from the fourth-order
249 finite difference scheme without applying any filtering technique. In the simulation using Ring Average,
250 the number of the averaging chunks in each azimuthal ring near the pole is set to be [18 18 18 18 36 36
251 36 36 72 72 72 72 144 144 144 144], from the first ring to the 16th ring, as indicated by the white circles
252 in the top panels around 80°N . For the FFT filter, a Fourier expansion is applied in the azimuthal direction
253 at each time step to the fluid density. Waves with frequencies that are higher than the cutoff frequencies
254 are eliminated from the Fourier spectra of prognostic variables. The values of prognostic variables are then



255 reconstructed through an inverse Fourier transform using the modified Fourier spectra. Each latitude grid
256 has its own cutoff frequency and the wave number to be cut off in this experiment near the pole is set to be
257 [1 1 2 2 2 2 4 4 4 4 8 8 8 8 10 10], which is similar to the TIE-GCM FFT filter spectrum [Wang, 1998].

258 As shown in Figures 4b-4c, density structures with large spatial gradient flow across the pole as time
259 progresses. Compared with the non-filter case in Figures 4h-4i, no evident numerical instability or arti-
260 ficial structure occurred when applying the Ring Average technique. In contrast, the density structure using
261 an FFT filter in Figures 4d-4f exhibits numerical oscillations in the radial direction, together with an arti-
262 ficial depletion of density near the pole. This density depletion is due to the non-conservative nature of
263 the FFT method by truncating high spatial frequency wave modes in a linear way. Figures 4j-4l show a
264 one-dimensional comparison of the density profiles along $x = 0.15$, with the region of averaging chunks
265 denoted by yellow. The comparisons suggest that the density flow is not noticeably affected by the imple-
266 mentation of the Ring Average technique in the finite difference solver. Note that the time step used after
267 applying the Ring Average technique is $0.0001 s$, which is 25 times larger than that used in the simulation
268 without Ring Average ($dt = 0.000004s$). Although the FFT filter can result in non-oscillatory solutions in
269 the finite-difference solver, however, as shown by the one-dimensional profiles in Figure 4l, evident density
270 oscillations occur near the pole due to numerical instability caused by the FFT method. The cut-off fre-
271 quency of FFT filter is case-dependent and have a problem of mass-loss, as compared to the Ring Average
272 method. The advection experiment illustrates that the Ring Average technique is capable of relaxing the
273 severe time step constraint and resolving large density gradient when passing through the clustered grid
274 cells near the pole.

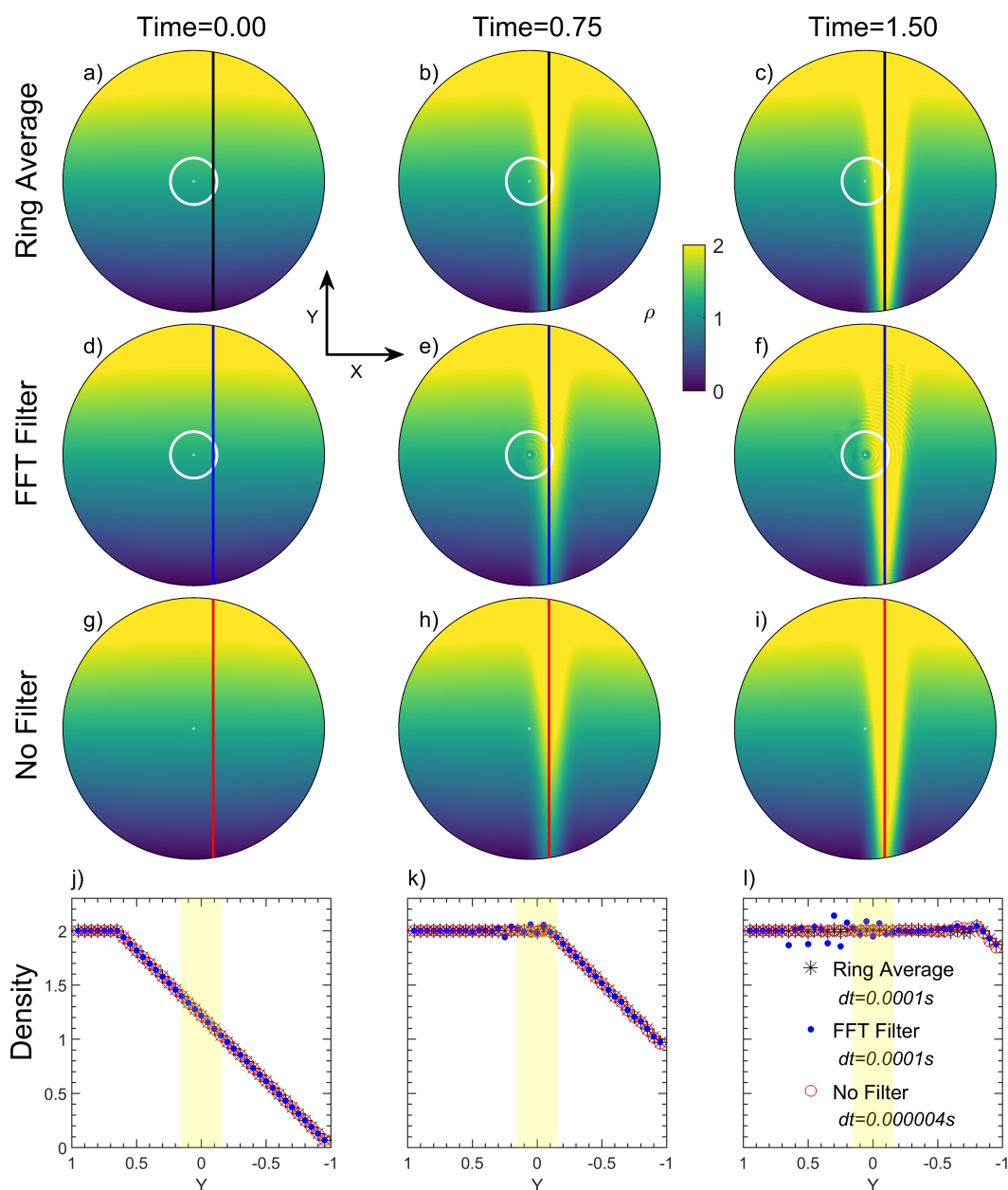


Fig 4 The distribution of density at three simulation snapshots ($t=0, 0.75$ and 1.5). The first three panels from top show the results with the Ring Average technique, with a FFT filter, and without any filter. The latitude boundaries of Ring Average and FFT filter are marked by white circles in the upper two panels. The bottom panels show the comparison of distributions of density along the line $x = 0.15$ (star) with Ring Average technique, (blue dot) with FFT filter, and (red circle) without filter at the three snapshots, respectively. The number of averaging chunks for the Ring Average technique in each azimuthal ring near the pole is set to be [18 18 18 18 36 36 36 36 72 72 72 72 144 144 144 144].



275 2.3 Ring Average for GCMs

276 We use the NCAR-TIE-GCM to demonstrate the effectiveness of the Ring Average technique in resolv-
 277 ing mesoscale upper atmospheric structures. TIE-GCM is a physics-based 3-D global model that solves
 278 the coupled equations of momentum, energy, and continuity for neutral and ion species of the upper atmo-
 279 spheric I-T system, using a fourth-order and centered finite difference scheme to evolve the advection terms
 280 on each pressure surface with a staggered vertical grid [Qian et al., 2014; Richmond et al., 1992; Roble
 281 et al., 1988]. The TIE-GCM utilizes a spherical coordinate system fixed with respect to the rotating Earth,
 282 with geographic latitude and longitude as the horizontal coordinates and pressure surface as the vertical
 283 coordinate. Following is a brief introduction of the basic equations in the TIE-GCM.

284 The thermospheric energy equation is

$$285 \frac{\partial T_n}{\partial t} = -\mathbf{V} \cdot \nabla T_n + \frac{ge^Z}{p_0 C_p} \frac{\partial}{\partial Z} \left\{ \frac{K_T}{H} \frac{\partial T_n}{\partial Z} + K_E H^2 C_p \rho \left[\frac{g}{C_p} + \frac{1}{H} \frac{\partial T_n}{\partial Z} \right] \right\} - w \left(\frac{\partial T_n}{\partial Z} + \frac{R^* T}{C_p \bar{m}} \right) + \frac{Q - L}{C_p}, \quad (25)$$

286 with temperature T_n , time t , the vertical coordinate $Z = \ln(p_0/p)$, the pressure p and p_0 the reference
 287 pressure. g is gravity, K_T is the molecular thermal conductivity, C_p is the specific heat per unit mass, H is
 288 the pressure scale height, K_E is the eddy diffusion coefficient, ρ is the atmospheric mass density, \mathbf{V} is the
 289 horizontal neutral velocity with the zonal and meridional components u_n and v_n , w is the vertical velocity
 290 defined by $w = dZ/dt$, R^* is the universal gas constant, \bar{m} is the mean atmospheric mass, and Q and L are
 291 the heating and cooling rates. The mean molecular mass \bar{m} is determined by

$$292 \bar{m} = \left[\frac{\Psi_{O_2}}{m_{O_2}} + \frac{\Psi_O}{m_O} + \frac{\Psi_{N_2}}{m_{N_2}} \right], \quad (26)$$

293 where Ψ and m represent the mass mixing ratio and the molecular mass for the three thermospheric major
 294 species O_2 , O , and N_2 , respectively.

295 The zonal momentum equation is expressed as

$$296 \frac{\partial u_n}{\partial t} = -\mathbf{V} \cdot \nabla u_n + \frac{ge^Z}{p_0} \frac{\partial}{\partial Z} \left(\frac{\mu}{H} \frac{\partial u_n}{\partial Z} \right) + \left(f + \frac{u_n}{R_E} \tan \lambda \right) v_n + \lambda_{xx} (u_i - u_n) \\ + \lambda_{xy} (v_i - v_n) - w \frac{\partial u_n}{\partial Z} - \frac{1}{R_E \cos \lambda} \frac{\partial \phi}{\partial \varphi}, \quad (27)$$



297 and the meridional momentum equation is

$$\begin{aligned} \frac{\partial v_n}{\partial t} = & -\mathbf{V} \cdot \nabla v_n + \frac{ge^Z}{P_0} \frac{\partial}{\partial Z} \left(\frac{\mu}{H} \frac{\partial v_n}{\partial Z} \right) - \left(f + \frac{u_n}{R_E} \tan \lambda \right) u_n + \lambda_{yy} (v_i - v_n) \\ & + \lambda_{yx} (u_i - u_n) - w \frac{\partial v_n}{\partial Z} - \frac{1}{R_E} \frac{\partial \phi}{\partial \lambda}, \end{aligned} \quad (28)$$

299 where λ and φ represent the geographic latitude and longitude, respectively. R_E is the radius of the Earth,
 300 μ is the viscosity coefficient which is the sum of eddy and molecular viscosity coefficients, f is the Coriolis
 301 parameter, ϕ is the geopotential, H is the pressure scale height, v_i and u_i are the meridional and zonal
 302 $\mathbf{E} \times \mathbf{B}$ ion drift velocities, and $\lambda_{xx}, \lambda_{xy}, \lambda_{yx}, \lambda_{yy}$ are the ion-drag tensor coefficients. The TIE-GCM “vertical
 303 velocity” $w = dZ/dt$ is determined by solving the continuity equation:

$$\frac{1}{r \cos \lambda} \frac{\partial}{\partial \lambda} (v_n \cos \varphi) + \frac{1}{r \cos \lambda} \frac{\partial u_n}{\partial \varphi} + e^Z \frac{\partial}{\partial Z} (e^{-Z} w) = 0. \quad (29)$$

305 The real vertical velocity is obtained by first integrating the continuing equation (29) over Z to get w , and
 306 then multiplying w by the neutral pressure scale height to get the right unit.

307 The thermospheric major species in the TIE-GCM includes O_2 , O , and N_2 . The continuity equation for
 308 the mass mixing ratio of O_2 and O is given by

$$\begin{aligned} \frac{\partial \tilde{\Psi}}{\partial t} = & -\mathbf{V} \cdot \nabla \tilde{\Psi} - \frac{e^Z}{\tau} \frac{\partial}{\partial Z} \left[\frac{\bar{m}}{m_{N_2}} \left(\frac{T_{00}}{T_n} \right)^{0.25} \tilde{\alpha}^{-1} L \tilde{\Psi} \right] + e^Z \frac{\partial}{\partial Z} \left[K(z) e^{-Z} \frac{\partial}{\partial Z} \left(1 + \frac{1}{\bar{m}} \frac{\partial \bar{m}}{\partial Z} \right) \tilde{\Psi} \right] \\ & + \tilde{S} - \tilde{R} - w \frac{\partial \tilde{\Psi}}{\partial Z}, \end{aligned} \quad (30)$$

310 where $\tilde{\Psi} = (\Psi_{O_2}, \Psi_O)$, τ is the diffusion time scale and equals to 1.86×10^3 s, m_{N_2} is the molecular mass
 311 for molecular nitrogen, $T_{00} = 273$ K is the standard temperature, $\tilde{\alpha}$ is the matrix operator of the diffusion
 312 coefficients, $K(Z)$ is the eddy diffusion coefficient, and \tilde{S} and \tilde{R} are the production and loss term for these
 313 two species. The diagonal matrix operator L has elements of the form

$$L_{ii} = \frac{\partial}{\partial Z} - \left(1 - \frac{m_i}{\bar{m}} - \frac{1}{\bar{m}} \frac{\partial \bar{m}}{\partial Z} \right), \quad (31)$$

315 where $i = 1, 2$ denote O_2 and O , respectively. The N_2 mass mixing ratio is determined by

$$\Psi_{N_2} = 1 - \Psi_{O_2} - \Psi_O. \quad (32)$$



317 The minor species in the TIE-GCM are $N(^4S)$, $N(^2D)$, and NO . The time scale of $N(^4S)$ is relatively
 318 short and thus is considered to be photochemical equilibrium. $N(^4S)$ and NO have longer life times so the
 319 transport effects must be taken into account. The governing equation for these two species is

$$320 \quad \frac{\partial \tilde{\Psi}}{\partial t} = -\mathbf{V} \cdot \nabla \tilde{\Psi} - e^z \frac{\partial}{\partial Z} \tilde{A} \left(\frac{\partial}{\partial Z} - \tilde{E} \right) \tilde{\Psi} + e^z \frac{\partial}{\partial Z} e^{-z} K_E(Z) \left(\frac{\partial}{\partial Z} + \frac{1}{\bar{m}} \frac{\partial \bar{m}}{\partial Z} \right) \tilde{\Psi} - w \frac{\partial \tilde{\Psi}}{\partial Z} + \tilde{S} - \tilde{R}, \quad (33)$$

321 where

$$322 \quad E = \left(1 - \frac{\tilde{m}}{\bar{m}} - \frac{1}{\bar{m}} \frac{\partial \bar{m}}{\partial Z} \right) - \tilde{\alpha} \frac{1}{T_n} \frac{\partial T_n}{\partial Z} + \tilde{F} \tilde{\Psi}, \quad (34)$$

323 where $\tilde{\Psi} = (\Psi_{NO}, \Psi_{N(^4S)})$, \tilde{A} is the vertical molecular diffusion coefficient, \tilde{S} and \tilde{R} are the production and
 324 loss terms for each species. Terms in \tilde{E} represent the effects of gravity, thermal diffusion and the frictional
 325 interaction with the major species on the vertical profiles of these two species. \tilde{F} is a matrix operator for the
 326 frictional interactions, $\tilde{\alpha}$ is the thermal diffusion coefficient, and \tilde{m} is the molecular mass for the two minor
 327 species.

328 The ions of the ionosphere in the TIE-GCM include O^+ , O_2^+ , NO^+ , N^+ , and N_2^+ , and the electron den-
 329 sity is calculated by chemical equilibrium of these ions. All major ionospheric ions except O^+ are assumed
 330 as photochemical equilibrium, thus their densities can be calculated simply by balancing the loss and pro-
 331 duction rates. The O^+ density is determined not only by O^+ loss and production but also by transportation
 332 due to $\mathbf{E} \times \mathbf{B}$ drifts, neutral winds, and field-aligned ambipolar diffusion. The O^+ continuity equation can
 333 be expressed as

$$334 \quad \frac{\partial n}{\partial t} = -\nabla \cdot (n\mathbf{V}) + Q - Ln, \quad (35)$$

335 where n is the O^+ density, Q is the production rate, L is the loss rate, and $\nabla \cdot (n\mathbf{V})$ is the transport term.
 336 The ion velocity is given by

$$337 \quad \mathbf{V} = \mathbf{V}_{\parallel} + \mathbf{V}_{\perp} \quad (36)$$

$$338 \quad \mathbf{V}_{\parallel} = \left\{ \mathbf{b} \cdot \frac{1}{\nu} \left[\mathbf{g} - \frac{1}{\rho_i} \nabla (P_i + P_e) \right] + \mathbf{b} \cdot \mathbf{U} \right\} \mathbf{b} \quad (37)$$

$$339 \quad \mathbf{V}_{\perp} = \frac{\mathbf{E} \times \mathbf{B}}{|\mathbf{B}|^2}, \quad (38)$$

340 where \mathbf{V}_{\parallel} and \mathbf{V}_{\perp} are the parallel and perpendicular velocities with respect to the magnetic field line caused
 341 by ambipolar diffusion and neutral winds, and $\mathbf{E} \times \mathbf{B}$ drifts, respectively, \mathbf{b} is a unit vector along the magnetic



342 field, ν is the ion-neutral collision frequency, \mathbf{g} is the acceleration due to gravity, ρ_i is the ion mass density,
343 P_i and P_e are the ion and electron pressures, respectively, \mathbf{U} is the neutral velocity, \mathbf{B} is the magnetic field,
344 and \mathbf{E} is the electric field.

345 By assuming a thermal quasi-steady state, the electron energy equation is

$$346 \quad \sin^2 I \frac{\partial}{\partial Z} \left(K^e \frac{\partial T_e}{\partial Z} \right) + \sum Q_e - \sum L_e = 0, \quad (39)$$

347 with I the geomagnetic dip angle, K^e the electron thermal conductivity parallel to the magnetic field, $\sum Q_e$
348 the sum of all local electron heating rates, and $\sum L_e$ the sum of all local cooling rates.

349 For the electrodynamics, i.e. the “neutral wind dynamo process”, TIE-GCM assumes a steady state
350 electrodynamics with a divergence free current density \mathbf{J} for longer time scales:

$$351 \quad \nabla \cdot \left[\sigma_P (\mathbf{E} + \mathbf{U} \times \mathbf{B}) + \sigma_H \mathbf{b} \times (\mathbf{E} + \mathbf{U} \times \mathbf{B}) + \mathbf{J}_{\parallel} + \mathbf{J}_{\mathbf{M}} \right] = 0, \quad (40)$$

352 where σ_P and σ_H are the Pederson and Hall conductivities, and \mathbf{U} is the neutral wind. \mathbf{J}_{\parallel} and $\mathbf{J}_{\mathbf{M}}$ are
353 the ohmic component of current density parallel to the magnetic field and the non-ohmic magnetospheric
354 component, respectively.

355 The ionospheric convection pattern for computing the plasma advection velocity \mathbf{V}_{\perp} at high latitudes
356 is specified by either the Heelis et al. [1982] or the Weimer [2005] empirical model, while at the bottom
357 boundary the migrating tides are specified using the Global-Scale Wave Model [Hagan and Forbes, 2002,
358 2003]. The current standard version of TIE-GCM (TIE-GCM v2.0) provides two spatial resolution options:
359 (1) $5^{\circ} \times 5^{\circ}$ in horizontal geographic latitude-longitude grid and 1/2 scale height in the vertical direction, and
360 (2) $2.5^{\circ} \times 2.5^{\circ}$ in horizontal geographic latitude-longitude grid and 1/4 scale height in the vertical direction.

361 In this study, the Ring Average technique is implemented in the TIE-GCM v2.0 to solve the issue of
362 clustering grid cells near the poles in the development of a high-resolution version of the TIE-GCM. This
363 technique is applied as a post-processing treatment of the fluid variables including oxygen ion density O^+ ,
364 neutral temperature T_n , thermospheric compositions Ψ , meridional, zonal, and vertical winds (U_n, V_n, w)
365 at each time step, with different reconstruction methods (PPM or PLM) for different variables (Table 1).
366 Due to the use of mpi parallelization in the TIE-GCM in supercomputers, the Ring Average technique
367 firstly collects the azimuthal data in the root thread, conducts the averaging-reconstruction process and
368 finally redistributes data into each mpi thread. Figure 5 illustrates Ring Average filters used in the main

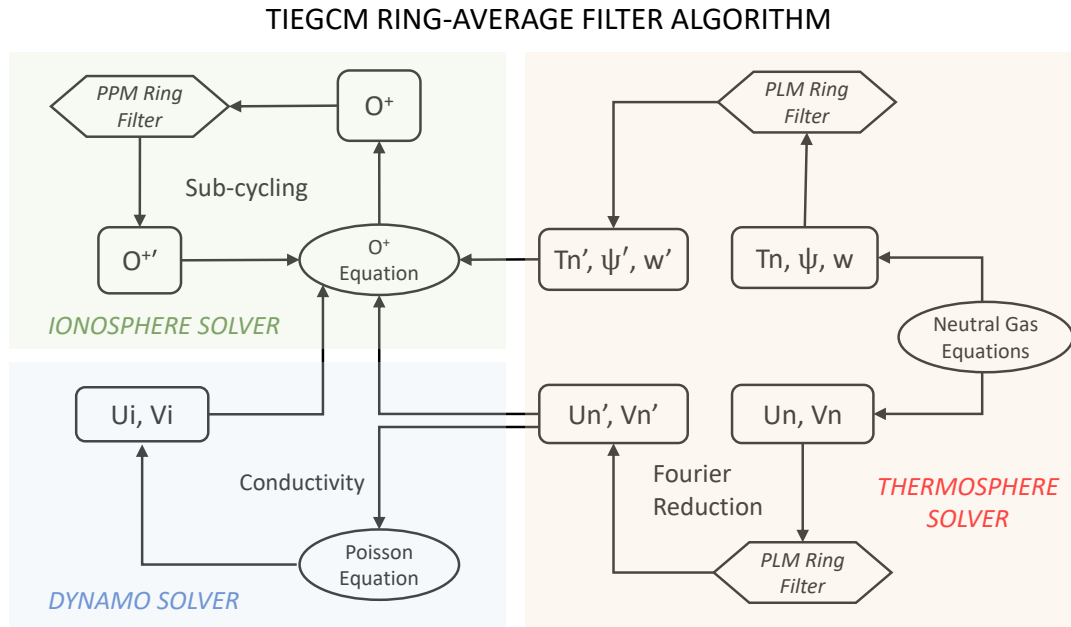


Fig 5 The main Ring Average Algorithm in the TIE-GCM

369 algorithms of the TIE-GCM, including the thermosphere solvers in Equations (25-34), the ionosphere solver
 370 for O^+ in Equations (35-39), and the dynamo solver for electrodynamic coupling in the Equation (40). For
 371 neutral variables in the thermosphere solver, the Ring Average technique with the PLM reconstruction
 372 method is utilized. Specifically, for the meridional and zonal neutral winds, the second and higher Fourier
 373 components are processed with the PLM Ring Average filter to maintain the direction of vectors across the
 374 pole, as displayed in Figure 5. The oxygen ion (O^+) in the ionosphere usually has much sharper gradients
 375 than the neutral variables, e.g., Tongue of Ionization (TOI) structures, thus the PPM method is used in the
 376 reconstruction process to provide high-order accuracy and handle the larger local gradient. Meanwhile, to
 377 balance the numerical stability and computational speed, a sub-cycling technique, which has a smaller time
 378 step for O^+ than neutral variables, has been applied in the O^+ solver, because the ions can move much faster
 379 than the neutrals with the ExB drifts especially during major geomagnetic storms.

380 On the basis of the Ring Average technique, a new high-resolution version of TIE-GCM with a hori-
 381 zontal longitude-latitude resolution as high as $0.625^\circ \times 0.625^\circ$ is developed. Table 2 lists the Ring Average
 382 setup used in different TIE-GCM resolutions. The third column in Table 2 represents the number of av-
 383 eraging chunks in each azimuthal ring near the pole, from the first innermost to the outermost rings. For



Table 1 The Basic Ring Average Settings of Variables (Column 1), and the corresponding Reconstruction Method (Column 2), Fourier Reduction (Column 3), and Sub-cycling (Column 4) in the TIE-GCM.

| Variables | Reconstruction Method | Fourier Reduction | Sub-Cycling |
|---|-----------------------|-------------------|-------------|
| $\Psi_O, \Psi_{O_2}, \Psi_{NO}, \Psi_{N(4S)}, w, T_n$ | PLM | No | No |
| U_n, V_n | PLM | Yes | No |
| O^+ | PPM | No | Yes |

Table 2 The Ring Average Setup for Different TIE-GCM Horizontal Resolutions (Column 1), Associated with the Number of Longitude Grids (column 2), and the Number of Averaging Chunks in each azimuthal ring near the pole (column 3).

| Horizontal Resolution | Number of Longitude Grids | Number of Chunks |
|----------------------------------|---------------------------|---|
| $2.5^\circ \times 2.5^\circ$ | 144 | [9,18,36,36,72,72,72,72] |
| $1.25^\circ \times 1.25^\circ$ | 288 | [9,9,18,18,36,36,36,36,72,72,72,72,144,144,144,144,144,144,144,144] |
| $0.625^\circ \times 0.625^\circ$ | 576 | [9,9,9,9,18,18,18,18,36,36,36,36,36,36,36,36,72,72,72,72,72,72,72,72,144,144,144,144,144,144,144,144,144,288,288,288,288,288,288,288,288] |

384 example, in the first azimuthal ring near the pole of the $0.625^\circ \times 0.625^\circ$ grid resolution, 64 longitude grids
 385 ($576/9 = 64$) and 40 longitude degrees ($360^\circ/9 = 40^\circ$) are grouped into a chunk. While in the outermost
 386 filtered ring (around 71.25° latitude), one averaging chunk only contains two longitude grids. Table 3 sum-
 387 marizes the information of different spatial resolutions of the TIE-GCM, including the current version of
 388 $2.5^\circ \times 2.5^\circ$ TIE-GCM with the default FFT filter, and $2.5^\circ \times 2.5^\circ$, $1.25^\circ \times 1.25^\circ$, and $0.625^\circ \times 0.625^\circ$ resolu-
 389 tion TIE-GCM with the Ring Average filter, respectively. As the resolution doubles, the time step decreases
 390 approximately linearly rather than quadratically. In practice, the $0.625^\circ \times 0.625^\circ$ resolution of the code runs
 391 about two times faster than real time with 256 processors on the NCAR/CISL Cheyenne supercomputer
 392 system (12 hours for one-day geomagnetic storm simulation), which is at fairly low computational cost for
 393 mesoscale-resolving global simulations. The preliminary results of the high-resolution TIE-GCM will be
 394 shown in the following section.

395 3 Applications

396 To show the capability of the new high-resolution TIE-GCM based on the Ring Average technique in
 397 resolving mesoscale I-T structures, we have simulated the ionospheric and thermospheric variations during
 398 the March 17, 2013 major geomagnetic storm as an example. Figure 6 displays the comparison of polar
 399 maps of electron densities between different filter techniques with the $2.5^\circ \times 2.5^\circ$ horizontal resolution.
 400 The electron density is plotted on pressure surface 2, which is near the F_2 region peak (~ 300 km altitude).



Table 3 Comparisons of Horizontal Resolution in Geographic Latitude-Longitude Grid (Column 1), Vertical Resolution (Column 2), Time Step (Column 3), O⁺ Sub-cycling Time Step (Column 4), and Polar Filter (Column 5) between Different TIE-GCM Versions^a.

| Horizontal Resolution | Vertical Resolution (Scale Height) | Time Step (s) | O ⁺ Sub-cycling Time Step (s) | Polar Filter |
|-----------------------|---------------------------------------|---------------|---|--------------|
| 2.5° × 2.5° | 1/4 | 60 | - | FFT |
| 2.5° × 2.5° | 1/4 | 60 | 5 | Ring Average |
| 1.25° × 1.25° | 1/4 | 20 | 2 | Ring Average |
| 0.625° × 0.625° | 1/4 | 10 | 0.1 | Ring Average |

^aIn columns 3-4, the time step corresponds to the cases of geomagnetic storms. The time step and sub-cycling time step would be more relaxed when the geomagnetic activity is quiet.

401 Figures 6a corresponds to the standard TIE-GCM with the FFT filter, while Figures 6b is the result using the
 402 Ring Average technique. Generally, the electron densities in two simulations in Figures 6a-6b are similar
 403 below 60°N, with an evident electron density enhancement seen in the afternoon sector and negative storm
 404 effects in the morning at 10:50 UT during the storm. The dense ionospheric plasma in the afternoon sector
 405 is transported in the anti-sunward direction into the polar cap region by the dusk cell of the convection
 406 pattern. Consequently, prominent polar tongue of ionization (TOI) features can be seen as a narrow density
 407 plume on the dayside, which stretches from 65°N at noon to latitudes greater than 80°N inside the polar cap.
 408 Those TOI features agree well with the polar Global Position System (GPS) total electron content (TEC)
 409 observations [e.g., Foster et al., 2005; Thomas et al., 2013]. It is evident that, in Figure 6a, the TOI cannot
 410 go through the polar cap region and generates an artificial “hole” structure at above 80°N. This non-physical
 411 depletion is associated with the loss of electron density induced by the removal of high frequency in the FFT
 412 filter, as also indicated in the advection experiment in Figure 4f. Consequently, the plasma within the TOI
 413 accumulates around the “hole” and a “ring-like” structure appears at about 70°N. In contrast, for the Ring
 414 Average technique, the electron densities in Figure 6b can successfully flow through the polar cap and arrive
 415 at the nightside, which is consistent with Figure 4c. Thus using the Ring Average, the artificial structures
 416 no longer exist in the polar cap region, indicating the advantage of Ring Average technique in handling the
 417 numerical instability by causing less artificial structures and preserving the real mesoscale structures.

418 Figure 7 shows the comparison of the polar maps of electron densities between simulations with differ-
 419 ent spatial resolutions using the Ring Average technique bolstered TIE-GCM. The simulation results after
 420 using the Ring Average technique are generally similar among different simulations, with finer structures
 421 in higher spatial resolutions. Besides the ionospheric parameters, we have also tested the performance of
 422 Ring Average in the thermospheric simulations (not shown here), which indicates that the thermospheric

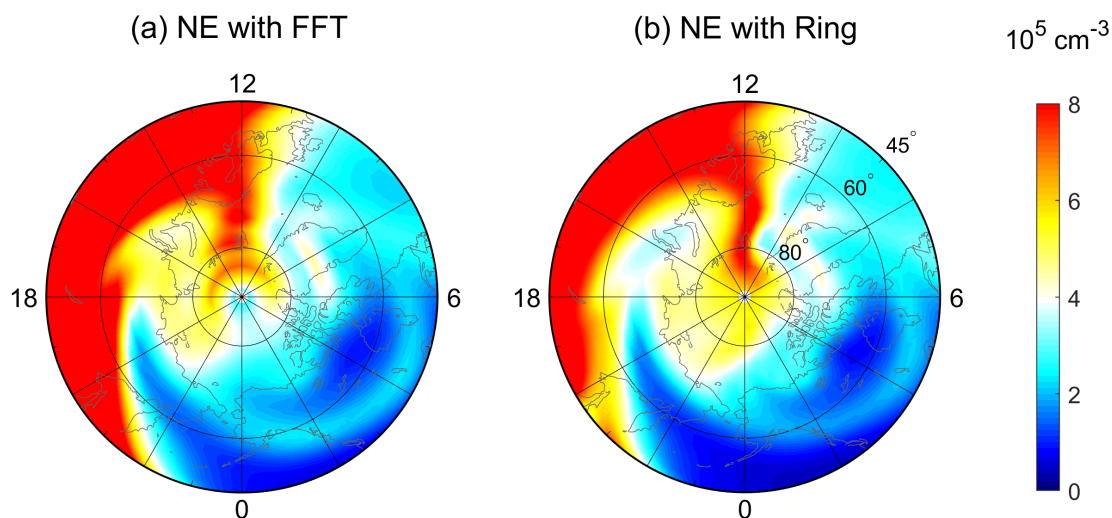


Fig 6 The simulated polar maps of electron densities using (left) FFT filter and (right) Ring Average at pressure surface 2 (near F_2 -region peak, ~ 300 km) at 10:50 UT on March 17, 2013 as a function of geographic latitude and local time. Both simulations have a horizontal resolution of $2.5^\circ \times 2.5^\circ$. The outer boundary is 45°N geographic latitude.

423 variables generally converge between different spatial resolutions. The thermospheric temperature, O/N_2 ,
424 and thermospheric density simulated by two kinds of filters do not show distinct differences as compared
425 with the ionospheric simulations, due to the relatively smoother variations of neutral parameters. Only
426 slight deviation exists locally on a smaller scale in the polar thermosphere. The results from Figures 6
427 and 7 demonstrate that the Ring Average technique can be applied in the finite difference method, which
428 is usually considered to be less stable than the finite volume scheme. The Ring Average method can suc-
429 cessfully maintain the numerical stability, even with the structures of large spatial gradients, and conserve
430 true mesoscale structures. Meanwhile, the Ring Average technique shows advantages of inexpensive com-
431 putational cost and easy implementation, as indicated by Table 3. By using the Ring Average, the time step
432 has been greatly relaxed in the ideal advection experiment and the high-resolution TIE-GCM, which would
433 maintain the computational cost to an acceptable level. Furthermore, the Ring Averaging can be applied
434 as a post filter after each simulation step and would not require a modification of the underlying code and
435 make the technique easily applied.

436 Benefiting from the Ring Average technique, the newly developed high-resolution TIE-GCM has been
437 applied to explore the mesoscale variations in the I-T system during space weather events. For instance,

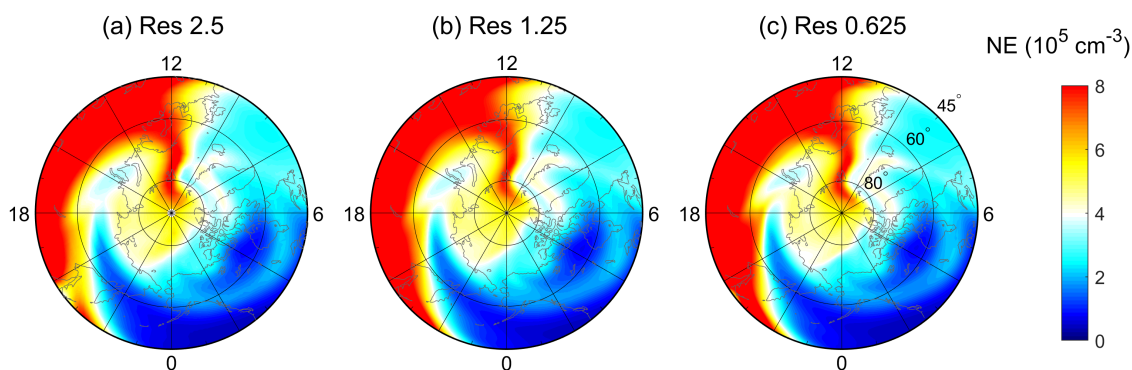


Fig 7 The polar maps of electron densities at pressure surface 2 (near the F_2 -region peak, ~ 300 km) at 10:50 UT on March 17, 2013 as a function of geographic latitude and local time for (a) $2.5^\circ \times 2.5^\circ$, (b) $1.25^\circ \times 1.25^\circ$, and (c) $0.625^\circ \times 0.625^\circ$ TIE-GCM horizontal resolutions using the Ring Average technique.

438 based on the $0.625^\circ \times 0.625^\circ$ high-resolution TIE-GCM simulations as well as satellite observations, Dang
439 et al. [2019] have reported the occurrence of double TOIs and carried out a comprehensive study on the
440 dynamic evolution and formation mechanism of double TOIs. Lu et al. [2020] used the high-resolution
441 model to study the ionospheric disturbances such as traveling ionospheric disturbances and storm enhanced
442 density during geomagnetic disturbances. Besides, the high-resolution TIE-GCM has also been utilized
443 to simulate the sub auroral polarization stream [Lin et al., 2019], neutral wind variabilities [Wu et al.,
444 2019], and the responses of the I-T system to solar eclipses [Dang et al., 2018a,b; Lei et al., 2018; Wang
445 et al., 2019]. These works highlight the enhanced capability of high-resolution TIE-GCM in resolving the
446 ionospheric and thermospheric mesoscale structures that is enabled by the Ring Average technique.

447 Simulating the mesoscale structures also requires a more realistic input from the upper and bottom
448 boundaries of the I-T system, corresponding to the electric field and auroral precipitation from the magne-
449 tosphere and the upward propagation of tides and waves from the lower atmosphere, respectively. In the
450 TIE-GCM, these inputs are directly adopted from two empirical models, the Weimer model and GSWM
451 model, which might not necessarily represent the complexity of the actual physical processes from the
452 boundaries. To obtain a more physical upper boundary condition, the CMIT has been developed [Wang
453 et al., 2004; Wiltberger et al., 2004] which couples the LFM global magnetosphere model with the I-T
454 model TIE-GCM. The LFM provides the TIE-GCM with high latitude electric fields and auroral electron
455 precipitations, and the TIE-GCM feeds ionospheric height-integrated conductance back to the LFM. The

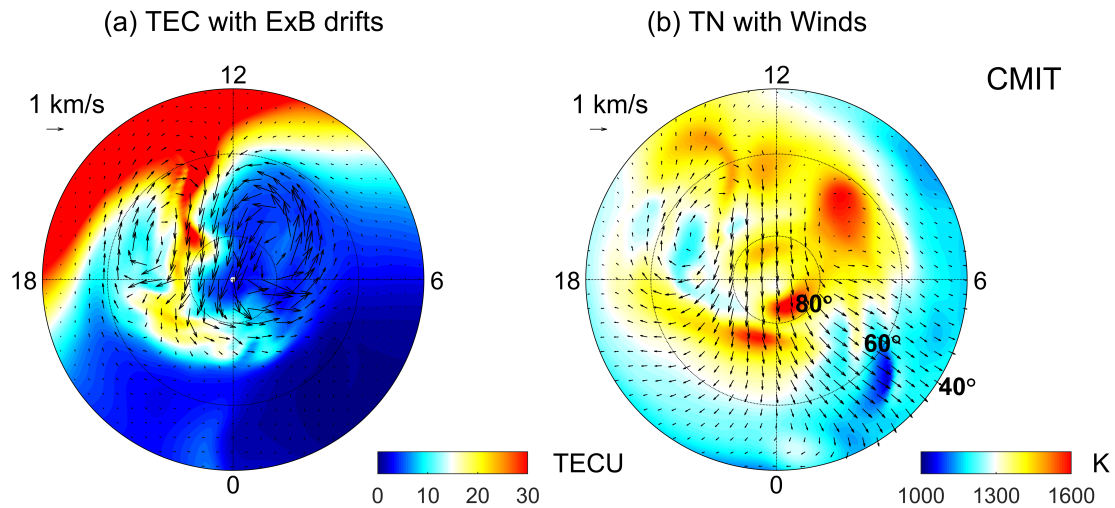


Fig 8 Polar maps of the (a) total electron content (TEC) and (b) neutral temperature simulated by CMIT as a function of geographic latitude and local time at 17:30 UT on March 17, 2013. The vectors represent the (a) $E \times B$ drifts and (b) horizontal neutral winds, respectively.

456 standard resolution of the ionosphere and thermosphere in CMIT is $2.5^\circ \times 2.5^\circ$ which is the same as the stan-
457 dard TIE-GCM. By implementing the high-resolution TIE-GCM in CMIT, the thermosphere-ionosphere
458 part in CMIT has a horizontal resolution of 1.25° in both latitude and longitude, which is comparable to
459 the magnetospheric resolution of 100 km mapped to the ionospheric reference altitude. Figure 8 shows an
460 example of CMIT simulation of the ionosphere and thermosphere, at 17:30 UT during the March 17, 2013
461 geomagnetic storm. The TEC in Figure 8a shows more dynamic and finer TOI variations driven by the
462 magnetospheric convection during the storm time. Meanwhile, the thermospheric temperature in Figure 8b
463 also exhibits distinct mesoscale structures, associated with changes in the neutral wind circulation and ion
464 collisional heating. The results illustrate that, with the implementation of the Ring Average technique, the
465 high-resolution CMIT show advantages in resolving the dynamic evolution of mesoscale structures in the
466 coupled magnetosphere-ionosphere-thermosphere system.

467 Furthermore, the Ring Average technique has also been applied in the WACCM-X which can provide
468 a relatively more realistic bottom boundary for the I-T simulation. The WACCM-X is a whole atmosphere
469 chemistry-climate general circulation model, spanning the range of altitude from the Earth's surface to the
470 upper thermosphere to simulate the entire atmosphere and ionosphere [Liu et al., 2018]. The ionosphere and
471 electrodynamic parts in WACCM-X are the same as in the TIE-GCM. The Ring Average scheme has been



472 successfully implemented in the O^+ transport module of the WACCM-X to get a higher spatial resolution
473 of the ionosphere. Figure 9 shows the simulation results of 2013 March 17, 2013 geomagnetic storm from
474 WACCM-X. For this simulation, the horizontal resolution is $1.25^\circ \times 0.9^\circ$ in longitude and latitude directions,
475 respectively, and the vertical resolution in the upper atmosphere is 1/4 of scale height. Detailed analyses and
476 exploration of the CMIT and WACCM-X results are beyond the scope of this study and will be studied in
477 the future. On-going efforts also include improving the resolution of vertical direction and electrodynamic
478 of the TIE-GCM and applying the Ring Average technique in high-resolution data assimilation and space
479 weather prediction.

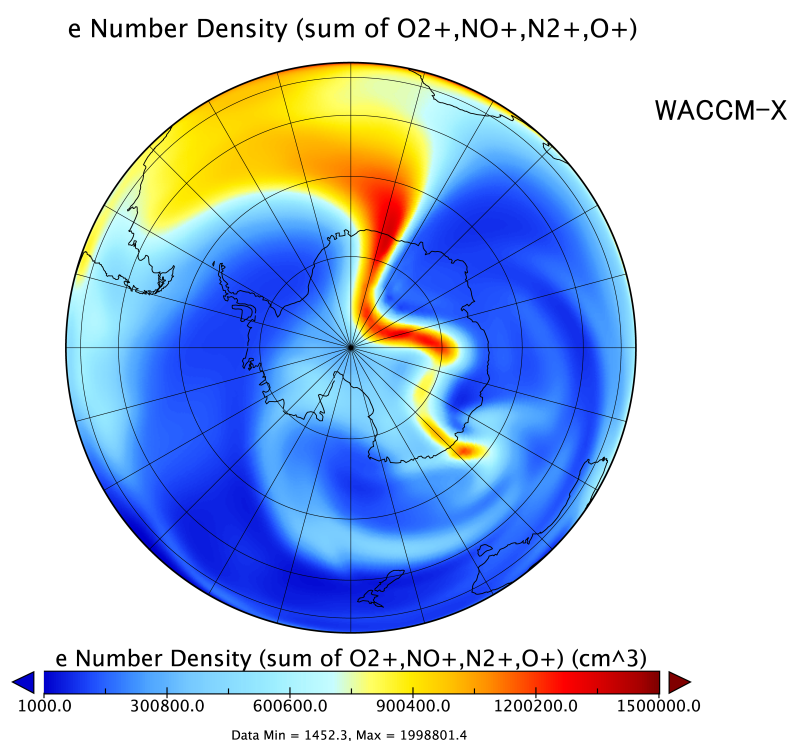


Fig 9 Polar map of the electron density in the Southern Hemisphere at 14:00 UT on March 17, 2013 from the WACCM-X 1° deg simulation.

480 **4 Summary**

481 In summary, a post-processing technique of averaging-reconstruction (Ring Average) algorithm is devel-
482 oped to solve the problem of clustering of azimuthal cells in a spherical coordinate with the finite difference



483 method. The Ring Average technique is conducted based on a reduced effective polar grid, by first averag-
484 ing quantities within azimuthal effective “chunks” and then re-constructing them within each chunk. The
485 Ring Average technique shows advantages of inexpensive computational cost, easy implementation, time
486 step relaxation, and maintenance of the mesoscale structures without introducing artifacts, which allows
487 for the development of high resolution GCMs to resolve mesoscale structures. We have developed a new
488 version of the TIE-GCM which has a horizontal resolution of $0.625^\circ \times 0.625^\circ$ in geographic longitude-
489 latitude grid by implementing the Ring Average technique as a post-process step. The non-physical “hole”
490 and “ring” structures, which are induced by FFT filter in the previous TIE-GCM version, no longer exist in
491 the high-resolution TIE-GCM associated with the Ring Average technique. The simulation results illustrate
492 that the high-resolution TIE-GCM is capable of resolving the mesoscale structures in the I-T system dur-
493 ing a geomagnetic storm event. Moreover, the Ring Average scheme has also been implemented in CMIT
494 and WACCM-X to enable a high spatial resolution self-consistent simulations of the whole geospace from
495 ground to the magnetosphere.

496 *Code Availability* The Ring Average technique and numerical experiments used in this study is available
497 at <https://doi.org/10.5281/zenodo.3719295>. The default TIE-GCM is developed by NCAR and is available
498 at <http://www.hao.ucar.edu/modeling/tgcm/tie.php>.

499 *Author contribution* TD developed the model code, performed the simulations and wrote the manuscript.
500 BZ, JL, and KS proposed the original idea and revised the manuscript. WW and AB helped to develop the
501 code and edited the manuscript. HL and KP contributed to couple the high-resolution TIEGCM to WACCM-
502 X and CMIT, respectively.

503 *Competing interests* The authors declare that they have no conflict of interest.

504 *Acknowledgments*

505 This work was supported by the B-type Strategic Priority Program of the Chinese Academy of Sciences
506 (XDB41000000), the National Natural Science Foundation of China (41831070, 41974181), and the Open
507 Research Project of Large Research Infrastructures of CAS - “Study on the interaction between low/mid-
508 latitude atmosphere and ionosphere based on the Chinese Meridian Project”. Dang T. was supported by
509 the National Natural Science Foundation of China (41904138), the National Postdoctoral Program for In-
510 novative Talents (BX20180286), the China Postdoctoral Science Foundation (2018M642525) and the Fun-
511 damental Research Funds for the Central Universities. HLL’s work was supported by the National Center



512 for Atmospheric Research, which is a major facility sponsored by the National Science Foundation un-
513 der Cooperative Agreement No. 1852977. The National Center for Atmospheric Research is sponsored
514 by the National Science Foundation. We would like to acknowledge high-performance computing support
515 from Cheyenne (doi:10.5065/D6RX99HX) provided by NCAR's Computational and Information Systems
516 Laboratory, sponsored by the National Science Foundation (NSF).

517 **References**

- 518 [1] S. Basu, S. Basu, J. J. Sojka, R. W. Schunk, and E. MacKenzie. Macroscale modeling and mesoscale
519 observations of plasma density structures in the polar cap. *Geophysical Research Letters*, 22(8):881–884,
520 1995.
- 521 [2] S. Bouaoudia and P. Marcus. Fast and accurate spectral treatment of coordinate singularities. *Journal of*
522 *Computational Physics*, 96(1):217–223, 1991.
- 523 [3] M. V. Codrescu, T. J. Fuller-Rowell, and J. C. Foster. On the importance of e-field variability for joule
524 heating in the high-latitude thermosphere. *Geophysical Research Letters*, 22(17):2393–2396, 1995.
- 525 [4] P. Colella and P. R. Woodward. The piecewise parabolic method (ppm) for gas-dynamical simulations.
526 *Journal of Computational Physics*, 54(1):174–201, 1984.
- 527 [5] R. Courant, K. Friedrichs, and H. Lewy. Über die partiellen differenzgleichungen der mathematischen
528 physik. *Mathematische annalen*, 100(1):32–74, 1928.
- 529 [6] G. Crowley, D. J. Knipp, K. A. Drake, J. Lei, E. Sutton, and H. Lühr. Thermospheric density enhance-
530 ments in the dayside cusp region during strong by conditions. *Geophysical Research Letters*, 37(7),
531 2010.
- 532 [7] T. Dang, J. Lei, W. Wang, A. Burns, B. Zhang, and S.-R. Zhang. Suppression of the polar tongue of
533 ionization during the 21 august 2017 solar eclipse. *Geophysical Research Letters*, 45:2918–2925, 2018a.
- 534 [8] T. Dang, J. Lei, W. Wang, B. Zhang, A. Burns, H. Le, Q. Wu, H. Ruan, X. Dou, and W. Wan. Global
535 responses of the coupled thermosphere and ionosphere system to the august 2017 great american solar
536 eclipse. *Journal of Geophysical Research: Space Physics*, 123(8):7040–7050, 2018b.



- 537 [9] T. Dang, J. Lei, W. Wang, B. Wang, B. Zhang, J. Liu, A. Burns, and Yukitoshi Nishimura. Formation
538 of double tongues of ionization during the 17 march 2013 geomagnetic storm. *Journal of Geophysical*
539 *Research: Space Physics*, 124, 2019.
- 540 [10] J. C. Foster, A. J. Coster, P. J. Erickson, J. M. Holt, F. D. Lind, W. Rideout, M. McCready, A. van
541 Eyken, R. J. Barnes, R. A. Greenwald, and F. J. Rich. Multiradar observations of the polar tongue of
542 ionization. *Journal of Geophysical Research: Space Physics*, 110:A09S31, 2005.
- 543 [11] K. Fukagata and N. Kasagi. Highly energy-conservative finite difference method for the cylindrical
544 coordinate system. *Journal of Computational Physics*, 181(2):478–498, 2002.
- 545 [12] T. J. Fuller-Rowell, D. Rees, S. Quegan, R. J. Moffett, M. V. Codrescu, and G. H. Millward. A coupled
546 thermosphere-ionosphere model (ctim). *STEP Report*, 239, 1996.
- 547 [13] M. E. Hagan and J. M. Forbes. Migrating and nonmigrating diurnal tides in the middle and upper
548 atmosphere excited by tropospheric latent heat release. *Journal of Geophysical Research*, 107(D24):
549 4754, 2002.
- 550 [14] M. E. Hagan and J. M. Forbes. Migrating and nonmigrating semidiurnal tides in the upper atmosphere
551 excited by tropospheric latent heat release. *Journal of Geophysical Research*, 108(A2):1062, 2003.
- 552 [15] R. A. Heelis, J. K. Lowell, and R. W. Spiro. A model of the high-latitude ionospheric convection
553 pattern. *Journal of Geophysical Research: Space Physics*, 87(A8):6339–6345, 1982.
- 554 [16] J. Lei, T. Dang, W. Wang, A. Burns, B. Zhang, and H. Le. Long-lasting response of the global
555 thermosphere and ionosphere to the 21 august 2017 solar eclipse. *Journal of Geophysical Research:*
556 *Space Physics*, 123(5):4309–4316, 2018.
- 557 [17] D. Lin, W. Wang, W. A. Scales, K. Pham, J. Liu, B. Zhang, V. Merkin, X. Shi, B. Kunduri, and
558 M. Maimaiti. Saps in the 17 march 2013 storm event: Initial results from the coupled magnetosphere-
559 ionosphere-thermosphere model. *Journal of Geophysical Research: Space Physics*, 124(7):6212–6225,
560 2019.
- 561 [18] H.-L. Liu, C. G. Bardeen, B. T. Foster, P. Lauritzen, J. Liu, G. Lu, D. R. Marsh, A. Maute, J. M. McIn-
562 ernerney, N. M. Pedatella, L. Qian, A. D. Richmond, R. G. Roble, S. C. Solomon, F. M. Vitt, and W. Wang.



- 563 Development and validation of the whole atmosphere community climate model with thermosphere and
564 ionosphere extension (waccm-x 2.0). *Journal Of Advances In Modeling Earth Systems*, 10(2):381–402,
565 2018.
- 566 [19] W. Lotko and B. Zhang. Alfvénic heating in the cusp ionosphere-thermosphere. *Journal of Geophysical*
567 *Research: Space Physics*, 123(12):10,368–10,383, 2018.
- 568 [20] G. Lu, I. Zakharenkova, I. Cherniak, and T. Dang. Large-scale ionospheric disturbances during the 17
569 march 2015 storm: A model-data comparative study. *Journal of Geophysical Research: Space Physics*,
570 125, 2020.
- 571 [21] H. Lühr, M. Rother, W. Köhler, P. Ritter, and L. Grunwaldt. Thermospheric up-welling in the cusp
572 region: Evidence from champ observations. *Geophysical Research Letters*, 31(6):L06805, 2004.
- 573 [22] J. G. Lyon, J. A. Fedder, and C. M. Mobarry. The lyon–fedder–mobarry (lfm) global mhd magneto-
574 spheric simulation code. *Journal of Atmospheric and Solar-Terrestrial Physics*, 66(15–16):1333–1350,
575 2004.
- 576 [23] J. J. Makela and Y. Otsuka. Overview of nighttime ionospheric instabilities at low- and mid-latitudes:
577 Coupling aspects resulting in structuring at the mesoscale. *Space Science Reviews*, 168(1):419–440,
578 2012.
- 579 [24] T. Matsuo and A. D. Richmond. Effects of high-latitude ionospheric electric field variability on global
580 thermospheric joule heating and mechanical energy transfer rate. *Journal of Geophysical Research:*
581 *Space Physics*, 113(A7), 2008.
- 582 [25] J. M. Prusa. Computation at a coordinate singularity. *Journal of Computational Physics*, 361:331–352,
583 2018.
- 584 [26] J. Purser. Degradation of numerical differencing caused by fourier filtering at high latitudes. *Monthly*
585 *weather review*, 116(5):1057–1066, 1988.
- 586 [27] L. Qian, A. G. Burns, B. A. Emery, B. Foster, Gang Lu, A. Maute, A. D. Richmond, R. G. Roble,
587 S. C. Solomon, and W. Wang. *The NCAR TIE-GCM: A community model of the coupled thermo-*
588 *sphere/ionosphere system*, pages 73–83. American Geophysical Union, Washington, DC, 2014.



- 589 [28] Z. Ren, W. Wan, and L. Liu. Gcitem-iggcas: A new global coupled ionosphere–thermosphere–
590 electrodynamic model. *Journal of Atmospheric and Solar-Terrestrial Physics*, 71(17-18):2064–2076,
591 2009.
- 592 [29] A. D. Richmond, E. C. Ridley, and R. G. Roble. A thermosphere/ionosphere general circulation model
593 with coupled electrodynamic. *Geophysical Research Letters*, 19(6):601–604, 1992.
- 594 [30] A. J. Ridley, Y. Deng, and G. Tóth. The global ionosphere–thermosphere model. *Journal of Atmo-*
595 *spheric and Solar-Terrestrial Physics*, 68(8):839–864, 2006.
- 596 [31] R. G. Roble, E. C. Ridley, A. D. Richmond, and R. E. Dickinson. A coupled thermosphere/ionosphere
597 general circulation model. *Geophysical Research Letters*, 15(12):1325–1328, 1988.
- 598 [32] W. C. Skamarock, J. B. Klemp, J. Dudhia, D. O. Gill, D. M. Barker, W. Wang, and J. G. Powers. A
599 description of the advanced research wrf version 3. ncar technical note-475+ str. 2008.
- 600 [33] L. Sun, J. Xu, W. Wang, X. Yue, W. Yuan, B. Ning, D. Zhang, and De M. Mesoscale field-aligned
601 irregularity structures (fais) of airglow associated with medium-scale traveling ionospheric disturbances
602 (mstids). *Journal of Geophysical Research: Space Physics*, 120(11):9839–9858, 2015.
- 603 [34] L. L. Takacs. *Filtering techniques on a stretched grid general circulation model*. National Aeronautics
604 and Space Administration, Goddard Space Flight Center, 1999.
- 605 [35] E. G. Thomas, J. B. H. Baker, J. M. Ruohoniemi, L. B. N. Clausen, A. J. Coster, J. C. Foster, and P. J.
606 Erickson. Direct observations of the role of convection electric field in the formation of a polar tongue
607 of ionization from storm enhanced density. *Journal of Geophysical Research: Space Physics*, 118(3):
608 1180–1189, 2013.
- 609 [36] W. Wang. *A thermosphere-ionosphere nested grid (ting) model*. PhD thesis, University of Michigan,
610 Ann Arbor, 1998.
- 611 [37] W. Wang, M. Wiltberger, A. G. Burns, S. C. Solomon, T. L. Killeen, N. Maruyama, and J. G. Lyon. Ini-
612 tial results from the coupled magnetosphere–ionosphere–thermosphere model: thermosphere–ionosphere
613 responses. *Journal of Atmospheric and Solar-Terrestrial Physics*, 66(15):1425–1441, 2004.



- 614 [38] W. Wang, T. Dang, J. Lei, S.-R. Zhang, B. Zhang, and A. Burns. Physical processes driving the
615 response of the f2 region ionosphere to the 21 august 2017 solar eclipse at millstone hill. *Journal of*
616 *Geophysical Research: Space Physics*, 124(4):2978–2991, 2019.
- 617 [39] D. R. Weimer. Improved ionospheric electrodynamic models and application to calculating joule
618 heating rates. *Journal of Geophysical Research: Space Physics*, 110:A05306, 2005.
- 619 [40] D. L. Williamson and G. L. Browning. Comparison of grids and difference approximations for numer-
620 ical weather prediction over a sphere. *Journal of Applied Meteorology*, 12(2):264–274, 1973.
- 621 [41] David L Williamson, John B Drake, James J Hack, Rüdiger Jakob, and Paul N Swartrauber. A standard
622 test set for numerical approximations to the shallow water equations in spherical geometry. *Journal of*
623 *Computational Physics*, 102(1):211–224, 1992.
- 624 [42] M. Wiltberger, W. Wang, A. G. Burns, S. C. Solomon, J. G. Lyon, and C. C. Goodrich. Initial re-
625 sults from the coupled magnetosphere ionosphere thermosphere model: magnetospheric and ionospheric
626 responses. *Journal of Atmospheric and Solar-Terrestrial Physics*, 66(15):1411–1423, 2004.
- 627 [43] Q. Wu, D. Knipp, J. Liu, W. Wang, R. Varney, R. Gillies, P. Erickson, M. Greffen, A. Reimer,
628 I. Häggström, G. Jee, and Y. Kwak. Hiwind observation of summer season polar cap thermospheric
629 winds. *Journal of Geophysical Research: Space Physics*, 124(11):9270–9277, 2019.
- 630 [44] B. Zhang, K. A. Sorathia, J. G. Lyon, V. G. Merkin, and M. Wiltberger. Conservative averaging-
631 reconstruction techniques (ring average) for 3-d finite-volume mhd solvers with axis singularity. *Journal*
632 *of Computational Physics*, 376:276–294, 2019.
- 633 [45] Q. H. Zhang, B. Zhang, M. Lockwood, H. Hu, J. Moen, J. M. Ruohoniemi, E. G. Thomas, S.-R. Zhang,
634 H. Yang, R. Liu, K. A. McWilliams, and J. B. H. Baker. Direct observations of the evolution of polar cap
635 ionization patches. *Science*, 339(6127):1597–1600, 2013.
- 636 [46] Q. Zhu, Y. Deng, A. Richmond, and A. Maute. Small-scale and mesoscale variabilities in the electric
637 field and particle precipitation and their impacts on joule heating. *Journal of Geophysical Research:*
638 *Space Physics*, 123(11):9862–9872, 2018.